36th AIAA Fluid Dynamics Conference and Exhibit
5 - 8 June 2006, San Francisco, California

AIAA 2006-3051

Laminar-Turbulent Transition of a Low Reynolds Number Rigid or Flexible Airfoil

Yongsheng Lian and Wei Shyy

Department of Aerospace Engineering

University of Michigan, Ann Arbor, MI, 48109

Abstract

Laminar-turbulent transition can affect the aerodynamic performance of low Reynolds number flyers, such as micro air vehicles (MAVs) which operate at the Reynolds number of 10^4-10^5. In order to gain better understanding of the fluid physics and associated aerodynamics characteristics, we have coupled (i) a Navier-Stokes solver, (ii) the e^N method transition model, and (iii) a Reynolds-averaged two-equation closure to study the low Reynolds number flow characterized with laminar separation and transition. A new intermittency distribution function suitable for low Reynolds number transitional flow is proposed and tested. To support the MAV applications, we investigate both rigid and flexible airfoils, which has a portion of the upper surface mounted with a flexible membrane, using SD7003 as the configuration. Good agreement is obtained between the prediction and experimental measurements regarding the transition location as well as overall flow structures. In the current transitional flow regime, though the Reynolds number affects the size of the laminar separation bubble, it does not place consistent impact on lift or drag. The gust exerts a major influence on the transition position, resulting in the lift and drag coefficients hysterisis. It is also observed that thrust instead of drag can be generated under certain gust condition. At $\alpha=4^o$, for a flexible wing, self-excited vibration affects the separation and transition positions; however, the time-averaged lift and drag coefficients are close to those of the rigid airfoil.

Nomenclature

c	Chord length
N	Critical factor in the transition model
H	Shape factor, δ^*/θ
Ti	Turbulence intensity
U	Freestream velocity
C_L	Lift coefficient
C_D	Drag coefficient
C_{Df}	Friction drag coefficient
δ	Boundary layer thickness
δ^*	Boundary layer displacement thickness
θ	Momentum thickness
u_τ	Friction velocity
μ	Molecular viscosity
ν_t	Kinematic eddy viscosity

Copyright © 2006 by authors. Published by the American Institute of Aeronautics and Astronautics, Inc., with permission.

k	Turbulent kinetic energy
ω	Specific dissipation rate, gust frequency
τ	nondimensionalized time =tc/U

Introduction

Micro air vehicles (MAVs), which refer to flight vehicle with a maximum dimension of 15 cm or less and an operating speed around 10 m/s, have attracted attention because of their expected broad applications and the challenging research topics involved. Three types of configurations have been explored in the MAV design, namely, fix wing design,[1,2] flapping wing design,[3,4] and rotary wing design. For MAVs with a linear dimension in the range of 10cm to 15cm, fixed wings are commonly adopted because fixed wings are simple in concept and easy to be implemented. However, fixed wing, as a miniature of large airplane wing, its performance is severally deteriorated as its operating Reynolds number drops to the range of 10^4 to 10^5. Under such low Reynolds number conditions, the boundary layer at the onset of the pressure rise may still be laminar, and thus is unable to sustain substantial adverse pressure gradients. For small angles of attack, the pressure gradient is modest, and the flow can remain laminar and attached; as the angle of attack increases, the adverse pressure gradients grows, and the flow experience separation on the upper surface. Depending on the specific situation, the separated flow may experience laminar-turbulent transition and reattach to form a laminar separation bubble. The laminar separation and the phenomena followed largely determine the MAV's aerodynamic performance. For this reason, fixed wing research focuses on the low Reynolds number aerodynamics, including the leading-edge separation bubble (LSB) and the thereafter incurred laminar to turbulence transition.

Ever since its first observation by Jones,[5] LSBs have been investigated by numerous researchers, as reviewed by Young and Horton.[6] Over a low Reynolds number airfoil, if the freestream turbulence intensity is low, flow starts as laminar; before transition the laminar boundary layer separates due to the adverse pressure gradient aft of the velocity peak. The separated flow quickly undergoes transition to become turbulent. Depending on the parameters such as the local Reynolds number, pressure gradient, surface roughness, and freestream turbulence intensity, the turbulent free shear layer may entrain enough high momentum fluid to reattach as a turbulent boundary layer behind a laminar separation bubble. Based on its effect on pressure and velocity distributions, LSB can form either a short bubble or a long bubble.[7] A short bubble covers a small portion of the airfoil surface and plays an insignificant rule in modifying the velocity and pressure distributions over an airfoil while a long bubble covers a considerable portion of the surface and modifies the inviscous pressure distribution and velocity peak. The presence of a bubble, especially a long one leads to substantial change in the effective airfoil shape, causing a decrease of lift and increase of drag, and consequently poor power efficiency.[8]

Aimed at improving the fixed-wing MAVs performance, numerous techniques have been proposed. A promising technique is to use flexible material as the lifting surface. This flexible wing concept was discussed by Shyy et al. [8] and Lian et al.[9], and has been practiced in the MAV design shown in Figure 1. It is observed from the wind tunnel experiment and flight test that a flexible wing can improve MAVs performance.[2] One advantage for the flexible wing is that it can facilitate passive shape adaptation, which results in delayed stall. It has been experimentally shown that under modest angles of attack, both rigid and membrane wings demonstrate similar lift characteristics with the stiffer wings having marginally higher lift coefficient.[10] However, the membrane wings stall at substantially higher angles of attack than rigid wings. This feature is a key element in enhancing the stability and agility of MAVs. For example, typical rigid wings have stall angles between 12 and 15 degrees, while flexible wings, which reduce their effective angle of attack due to the surface deformation,[11] have stall angles between 30 and 45 degrees.

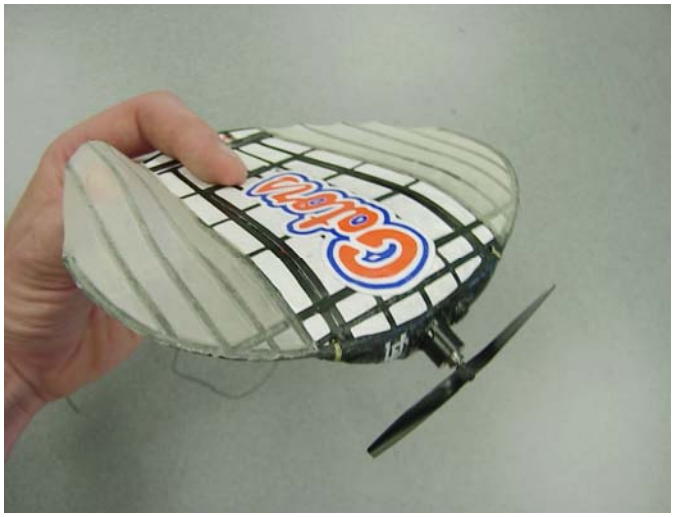

Figure 1. MAV designs with fixed wing at the University of Florida (Ifju et al. [2])

Because the onset of transition is affected by a wide spectrum of disturbance, such as pressure gradient, wall roughness, freestream turbulance, acoustic noise, wall heating or cooling, wall suction or blowing, etc., a comprehensive transition model considering all these factors is not yet available. Even if we limit our focus on freestream turbulence, it is still a challenge to give an accurate mathematical description. In the general area of transition study, approaches of transition prediction range from simple empirical methods through those based on parallel and linear stability theories, such as the e^N methods,[12,13] to linear or nonlinear parabolized stability equations (PSE), to more comprehensive methods such as the Navier-Stokes models. To date, each of the proposed methods deals with only one or two of those factors affecting the transition.

In the study of LSB, there are some empirical methods to predict transition. Most of them are devised based on collective experimental measurements. For example, Roberts,[14] Davis et al.,[15] and Volino and Bohl[16] proposed models which estimate the transition length typically based on the turbulence level at boundary layer edge at the separation; Mayle[17], Praisner and Clark,[18] and Roberts and Yaras[19] put forth models which predict the transition length using the local Reynolds number based on the momentum thickness. These models tend to oversimplify the downstream factors such as pressure gradient, surface geometry, and surface roughness. For the attached flow Wazzen et al.[20] proposed a model based on the shape factor H. His model gives a unified correlation between the transition point and Reynolds number for a variety of problem. For separated flow, however, there is no similar model. It is probably due to the limited availability of accurate shape factor measurement, which, in order to account for flow separation, need to consider the flow reversal, which is challenging.

There are other approaches of predicting transition based on stability theory and boundary layer theory. Among them the e^N method has been adopted by multiple researchers.[12,13,21,22] The e^N method is based on the linear stability analysis and boundary layer theory. It solves the Orr-Sommerfeld equation to evaluate the local growth rate of unstable waves based on the velocity and temperature profiles over the body. Transition occurs when the amplification of most unstable Tollmien-Schlichting (TS) wave reaches certain value. Its application can be found in the coupled inviscid-boundary model such as that employed in XFOIL.[23] XFOIL employs the steady Euler equations in integral form to represent the inviscid flows, a two-equation integral formulation based on dissipation closure to represent boundary layers and wakes, and e^N methods to tackle transition.

More sophisticate approaches have also been proposed. For example, Holloway et al. used unsteady Reynolds-averaged Navier-Stokes (RANS) model to study the flow separation over a blunt body for the Reynolds number range of 10^4 to 10^7.[24] For the flat plate case, as illustrated by Dick and Steelant.[25], the transition points seem to be predicted earlier than indicated by the experiment. Edwards et al.[26] developed a unified one-equation model by blending an eddy-viscosity-transport equation[27] with the standard Spalart-Allmaras one-equation turbulence model.[28] To improve the predictive capability, Wilcox devised a low-Reynolds number k-ω turbulence model to predict transition.[29] Steelant and Dick,[30] Suzen and Huang, [31] and Suzen et al. [32] incorporated the concept of intermittency factor to model the transitional flows. This can be achieved either by using conditioned Navier-Stokes equations or by multiplying the eddy viscosity by the intermittency factor. In all cases the intermittency factor is solved from a transport equation, which is based on empirical correlations. More importantly, the onset of transition is determined by empirical correlations. Zheng et al.[33] presented another approach by coupling the Wilcox's low Reynolds number k-ω model with a sensor technique. In their study the introduced sensor, which is a function of streamline curvature, is introduced to detect separation and trigger transition. The rationale is to increase the eddy viscosity in the circulation zone. Therefore, the result is sensitive to the topology of the separation bubble. As to be presented, based on the SD7003 airfoil,[34] we have found that this method works well for short separation bubble but under-predicts the length of long bubble.

The concept of coupling RANS solver and e^N method to predict transition has been practiced by Radespiel et al.[35] and Stock and Haase.[36] More recent application can be found in the work of Yuan et al.[37] Successful application of this coupled approach needs the following assumptions: 1) the velocity profiles are two dimensional and steady; 2) the initial disturbance is infinitesimally small; 3) the boundary layer is thin. Even though in practice the e^N method has been extended to study the three-dimensional flow,[38] the physical meaning of the envelope method is not clear. Furthermore, even in two-dimensional flow, as will be presented, not all these assumptions can be satisfied.[33]

The large eddy simulation (LES)[39] and direct numerical simulation (DNS) are being employed to study laminar-turbulent transition. For example, Yang and Voke[40] investigated boundary layer separation and transition employing LES. Yuan et al.[37] studied transition over a low-Reynolds number airfoil using LES. However, given the complexity of the transition physics and the need for accounting for complex geometry in practice, the e^N method is expected to remain a practical approach for engineering applications.

In the present work we simulate the transitional flow by coupling an incompressible RANS solver with the e^N method. The building block of this approach compromises a fluid solver, the e^N method, and a turbulence model. The e^N method is based on the work by Drela and Giles.[23] Upstream of the transition point, the laminar form of the Navier-Stokes equations are solved along with the transition detection scheme. Downstream of the transition point, Wilcox's k-ω turbulence model is used as the turbulence closure.[29] Both rigid and flexible wings are investigated in order to aid MAV design. This paper is structured as follows: first, we present geometric description of the chosen airfoil and the recent experimental work with this airfoil; second, we introduce the major modeling and numerical approaches employed in this work; third, we present the numerical results and discuss the outcome. We will first validate our transitional model against available experimental data, and examine the effects of angle of attack, freestream turbulence intensity, Reynolds number, and gust on the transition behavior and the airfoil performance. Then, we investigate the issues by considering the transitional flow over a flexible airfoil.

Experimental Study of SD7003 Airfoil

We adopt the SD7003 airfoil[34] in the present work to study LSB and transition. The airfoil has a maximum thickness of 8.5% and a maximum camber of 1.48%. The geometry is shown in Figure 2. This airfoil has received substantial experimental investigations. It exhibits a long, stable LSB over a broad range of angle of attack at Reynolds numbers below 10^5.[41] Recently three groups, namely Hanff at the Institute for Aerospace Research (IAR),[42] Nerger et al. at the Technical University of Braunschweig (TU-BS),[43] and Ol et al. at Air Force Research Lab (AFRL),[41] have used SD7003 airfoil to experimentally study LSB and transition. A

detailed comparison of instruments and experimental results can be found in the work of Ol et al.[41] Here we briefly summarize their facilities and major observations. Table 1 compares the tunnel types and particle image velocimetry (PIV) resolutions. Among the three, the work by Nerger et al. [43] has the highest resolution.

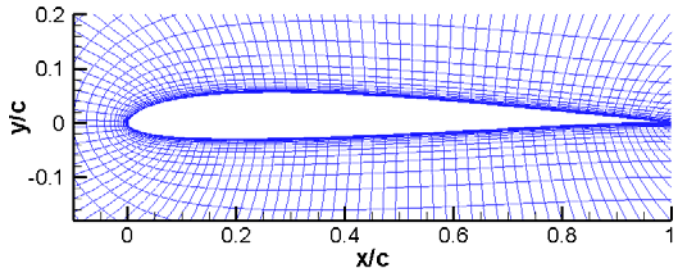

Figure 2. SD7003 airfoil with 8.5% thickness and 1.4% camber.

For the work of Hanff[42] and Nerger et al., [43] measurements were taken for Reynolds number of 60,000 and angle of attack of 4°; Ol et al. [41] took one more step and extended their measurement to other angles of attack. The locations of separation, transition onset, time-averaged reattachment, and maximum bubble height at the angle of attack of 4 degree are listed in Table 2, along with the estimated facility turbulence intensity.

Table 1. Comparison of PIV resolution for the three data sets[41]

Group	Tunnel type	Window Width [pix] (%chord)	Vector Spacing [pix] (%chord)
Hanff[42]	Tow Tank	16 (0.46%)	4 (0.12%)
Nerger et al. [43]	Wind Tunnel	16 (0.16%)	8 (0.085%)
Nerger et al. [43]	Water Tunnel	32 (0.32%)	8 (0.085%)
Ol et al. [41]	Water Tunnel	32 (0.44%)	16 (0.22%)

Table 2 Measured and computed SD7003 LSB properties at Re=60,000 and 4° angle of attack. Here c is the airfoil chord length.

Group	Freestream turbulence level Ti[%]	Separation positon x_s/c	Transition position x_t/c	Reattachment position x_r/c	Max Bubble Height, h_b/c
Hanff[42]	0.0	0.33	0.57	0.63	0.027
Nerger et al. [43]	0.1	0.30	0.53	0.62	0.028
Ol et al. [41]	~0.1	0.18	0.47	0.58	0.029

Regardless of the differences in the freestream turbulence, the maximum bubble heights measured in different experiments agree well with each other. The data on the LSB separation, transition, and reattachment points agree well between the measurement of Hanff[42] and Nerger et al. [43] while Ol et al. [41] predicts that the flow separates and reattaches further upstream. The reason, as explained by Ol et al. [41] is that in his experiment the true angle of attack may be slightly larger than the correct value. Nevertheless, the data by Ol et al. [41] closely match the XFOIL prediction.

The measured lift coefficient by Ol et al. [41] is in line with the measurement by Selig et al.[34] and XFOIL data at modest angles of attack. While XFOIL works well at modest angles of attack, it doesn't follow the fluid physics when the flow separates massively.

Numerical Methods

Reynolds-Averaged Navier-Stokes Solver

We simulate the transitional flow by solving the incompressible Navier-Stokes equations coupled with a transition model. The equations are written in three-dimensional curvilinear coordinates and are solved with a pressure-based algorithm, generalizing from the original Semi-Implicit Method for Presure-Linked Equations (SIMPLE).[44,45] We discretize the convection terms with the second-order upwind scheme and discretize the diffusion terms with second-order central difference scheme. The time integration is performed with an implicit three-point backward scheme for better handling of accuracy and strict time step constraint imposed by the extremely fine grid resolution. We use Wilcox's k-ω turbulence model[46] as the turbulence closure. For clarity, the turbulence model is written in Cartesian coordinates as follows:

$$\frac{\partial k}{\partial t}+\frac{\partial (u_j k)}{\partial x_j}=\frac{\tau_{i,j}}{\rho}\frac{\partial u_i}{\partial x_j}-\beta^*\omega k+\frac{\partial}{\partial x_j}[(\nu+\sigma^*\nu_T)\frac{\partial k}{\partial x_j}], \tag{1}$$

$$\frac{\partial (\rho\omega)}{\partial t}+\frac{\partial (u_j \omega)}{\partial x_j}=\frac{\alpha\omega}{k}\frac{\tau_{i,j}}{\rho}\frac{\partial u_i}{\partial x_j}-\beta\omega^2\frac{\partial}{\partial x_j}[(\nu+\sigma\nu_T)\frac{\partial \omega}{\partial x_j}]$$

where

$$\nu_T=\alpha^* k/\omega, \quad \tau_{i,j}=2\rho\nu_T S_{i,j}-2/3\rho k\delta_{i,j}, \quad S_{ij}=\frac{1}{2}(\frac{\partial u_i}{\partial x_j}+\frac{\partial u_j}{\partial x_i}), \tag{2}$$

$$\alpha^*=\frac{\alpha_0^*+\mathrm{Re}_T/R_k}{1+\mathrm{Re}_T/R_k}, \quad \alpha=\frac{13}{25}\frac{\alpha_0+\mathrm{Re}_T/R_\omega}{1+\mathrm{Re}_T/R_\omega}\frac{1}{\alpha^*}, \quad \beta^*=\frac{9}{100}\frac{4/15+(\mathrm{Re}_T/R_\beta)^4}{1+(\mathrm{Re}_T/R_\beta)^4}, \tag{3}$$

$$\mathrm{Re}_T=\frac{k}{\omega\nu}, \quad \beta=\frac{9}{125}, \quad \sigma^*=\sigma=\frac{1}{2}, \quad \alpha_0^*=\frac{1}{3}\beta, \quad \alpha_0=\frac{1}{9}, \tag{4}$$

$$R_\beta=8, \quad R_k=6, \quad R_\omega=2.95. \tag{5}$$

For the preceding equations, the value of turbulence kinetic energy k at the freestream is set based on the experimental data. Because there is no direct measurement for the dissipation rate, we assign a value of ω so that the resulting turbulence kinetic eddy viscosity $\nu_t=k/\omega$ is much smaller than the laminar kinetic viscosity. On the wall surface, the kinetic energy is set to zero, and the dissipation rate follows:

$$\omega=u_\tau^2 S_R/\nu, \tag{6}$$

where u_τ is the friction velocity, and we set S_R to 500 to simulate the smooth wall.

Transition Model

The transition prediction method employed here is based on the Orr-Sommerfeld equation, which is the essence of the e^N method.[12,13] Specifically, the e^N method is based on linear stability analysis and it states that transition occurs when the most unstable TS wave in the boundary layer has been amplified by a factor e^N:

$$N=\max_\omega \tilde{n}(x_t;\omega) \qquad \tilde{n}(x;\omega)=-\int_{x_0}^{x}\alpha_i(\omega)dx \tag{7}$$

where ω is the frequency, $x_0(\omega)$ is the onset location of instability, $-\alpha_i$ the spatial growth rate of the TS wave, and $n(x;\ldots)$ describes the amplitude growth of the disturbance along the chord of the airfoil. Given a

velocity profile, the local disturbance growth rate can be determined by solving the Orr-Sommerfeld eigenvalue equation. And then the amplification factor is calculated by integrating the growth rate, usually the spatial growth rate, starting from the point of neutral stability. Gleyzes et al.[47] found that the integrated growth rate can be approximated by straight lines as follows:

$$\tilde{n} = \frac{d\tilde{n}}{d\,\mathrm{Re}_\theta}(H_k)[\mathrm{Re}_\theta - \mathrm{Re}_{\theta_0}(H_k)]\,. \tag{8}$$

With this approach, we can approximate the amplification factor with a relatively good accuracy without solving the eignevalue equations. And this approach is adopted by Drela and Giles.[23] For similar Blasius flow, the amplification factor $\tilde{n}$ is determined by the following empirical formula:

$$\frac{d\tilde{n}}{d\,\mathrm{Re}_\theta} = 0.01\{[2.4H_k - 3.7 + 2.5\tanh(1.5H_k - 4.65)]^2 + 0.25\}^{1/2} \tag{9}$$

For nonsimilar flow, based on the properties of the Falkner-Skan profile family, the amplification factor with respect to the spatial coordinate ξ is expressed as:

$$\frac{d\tilde{n}}{d\xi} = \frac{d\tilde{n}}{d\,\mathrm{Re}_\theta}\frac{1}{2}\left(\frac{\xi}{u_e}\frac{du_e}{d\xi}+1\right)\frac{\rho_e u_e \theta^2}{u_e \xi}\frac{1}{\theta}, \tag{10}$$

An explicit expression for the integrated amplification factor then becomes

$$\tilde{n}(\xi) = \int_{\xi_0}^{\xi}\frac{d\tilde{n}}{d\xi}d\xi\,, \tag{11}$$

where ξ_0 is the point where $\mathrm{Re}_\theta = \mathrm{Re}_{\theta_0}$, and the critical Reynolds number are expressed by the following empirical formulas:

$$\log_{10}\mathrm{Re}_{\theta_0} = \left(\frac{1.415}{H-1} - 0.489\right)\tanh\left(\frac{20}{H-1} - 12.9\right) + \frac{3.295}{H-1} + 0.44\,, \tag{12}$$

As already mentioned, the e^N method requires that the following assumptions be satisfied:

1. The initial disturbance is infinitesimally small.
2. The laminar boundary layer is thin and gradually grows in the streamwise direction.

While the second assumption seems stringent to the LSB study, the DNS simulation shows that the assumption of parallel flow needed for the linear stability computations is largely satisfied for a broad range of LSBs.[35,37]

The freestream intensity effect can be incorporated into the e^N method by the following correlation proposed by Mack[48]

$$N = -8.43 - 2.4\ln(T_i), \qquad 0.0007 \le T_i \le 0.0298 \tag{13}$$

van Ingen [49] also proposed similar formula. Due caution should be taken when we use those correlations. The freestream turbulence level itself is not sufficient to describe the disturbance. Information about the distribution across the frequency spectrum should also be considered. The so-called "receptivity", i.e., how the initial disturbances within the boundary layer are related to the outside disturbances, is a critically important issue. Actually, we can only determine the N factor if we know the "effective T_i", which can only be defined through a comparison of measured transition position with calculated amplification ratios.[49] Mack's correlation is used throughout our work.

Before the transition point, the RANS equations together with the k-ω turbulence model are solved without the turbulent production terms; after transition, the production term is switched on. In the literature a variety of intermittency distribution functions are proposed.[50] For example, Cebeci[51] improved the intermittency

distribution function of Chen and Thyson[52] to compass a low Reynolds number range from 2.4×10^5 to 2×10^6 with laminar separation bubble. However, no model is available when the Reynolds number is less than 10^5. We gather that for separation caused transition at such low Reynolds number conditions, the intermittency distribution is largely determined by the length from the separation point to the transition point, the shorter the length, the quicker flow becomes turbulence. Also, previous work suggests that the flow property at the transition point will also be important. Based on the available experimental data and our simulation, we suggest the following model:

$$\gamma = \begin{cases} 1-\exp(-\left(\left(\dfrac{\max(H_T-2.21,0)}{20}\right)^2-1\right)\left(\dfrac{x-x_T}{x_T-x_S}\right)^2 \mathrm{Re}_{\theta T}) & (x \ge x_T) \\ 0 & (x < x_T) \end{cases} \tag{14}$$

where x_T is the transition onset position, x_S is the separation position, H_T is the shape factor at the transition onset, and $Re_{\theta T}$ is the Reynolds number based the momentum thickness at the onset point of transition. It will show later that the numerical results based on the proposed function have an agreement with the experiment measurement.

The Structural Model

In the design shown in Figure 1 the top surface of the wing is covered by latex membrane. To simulate the flow over such a flexible surface, we need a structural solver to model the transient behavior of the structure. A dynamic membrane model proposed by Lian et al.[53] is adopted here. In the model the membrane material is assume to obey the hyperelastic Moody-Rivlin model. For an initially isotropic membrane, Green and Adkins [54] show that there exits a strain energy function W which can be expressed as the following form

$$W = W(I_1, I_2, I_3) \tag{15}$$

where I_1, I_2, and I_3 are the first, second, and third invariants of the Green deformation tensor. If the material is incompressible, namely, $I_3 = 1$, then the strain energy is a function of I_1 and I_2 only. The following linear form has been found valuable in the study of such a membrane

$$W = c_1(I_1 - 3) + c_2(I_2 - 3) \tag{16}$$

where c_1 and c_2 are the two material parameters. Moody-Rivlin model is one of the most frequently employed hyperelastic models because of its mathematical simplicity and relatively good accuracy for reasonably large strains (less than 150 percent).[55]

The finite element procedure is based on the principle of virtual work. A triangular element is employed. The system of governing equations for membrane responses under external load can be formulated as follows:

$$\mathbf{M}\ddot{\mathbf{D}}(t) + \mathbf{F}^{\text{int}} = \mathbf{F}^{\text{ext}} \tag{17}$$

where **M** is a positive definite mass matrix, which remains constant, **D**(t) represents the nodal displacement vector in global coordinates, $\ddot{\mathbf{D}}(t)$ is the nodal acceleration vector, $\mathbf{F}^{\text{int}}$ is the internal force, and $\mathbf{F}^{\text{ext}}$ is the external load. To integrate the system of equations (17) we adopt the widely used implicit Newmark's family of methods.[56]

Moving Grid Technique

In our study we need to dynamically update the computational grid to accommodate the geometrical change of the flexible structure. The moving grid technique adopted here is based on the spring analogue methods and master-slave concept. This approach maintains a point-matched grid block interface while preserving grid quality and preventing potential grid cross-over.[57] Since the grid speed is typically not prescribed analytically, numerical estimation is necessary. Furthermore, one should employ formulas consistent between the time stepping treatment of the primary variables, the grid speed, and the geometric quantities. Both first-

and second-order schemes have been employed. For example, Visbal and Gaitonde[58] have adopted the following 3-level, second-order scheme

$$\dot{x} = \frac{3x^{n+1} - 4x^{n} + x^{n-1}}{2\Delta t}, \tag{18}$$

where the superscripts $^{n+1}$, ^{n}, and $^{n-1}$ refer to the current time instant, and the past two consecutive time instants, respectively. The Jacobian matrix needs to be updated by enforcing the geometric conservation law.[59]

Results and Discussion

Our numerical simulations follow the set up of Ol et al.[41] The geometry is the SD7003 airfoil, which exemplifies LSB at low Reynolds number conditions. The fluid has density ρ of 1,000 [kg/m^3] and laminar viscosity μ of 0.001 [kg/m*s]. The freestream velocity U_0 is 0.3 [m/s]. Based on freestream velocity and airfoil chord length of 20 cm the Reynolds number is 60,000. In the experiment the freestream turbulence intensity Ti is set to around 0.1%. In our computations, we initialize the turbulence kinetic energy based on formula k=3/2$(TiU_0)^2$. Because the dissipation rate information is not available from the experiment, we employ a crude way to set the dissipation rate so that at the freestream the turbulent viscosity μ_t is much less than the laminar viscosity.

Grid Sensitivity Analysis

To minimize the boundary condition effects, we set the outer boundary 25 chords away from the airfoil. Close to the wall we strive to ensure that there are at least 30 grid points within the boundary layer before separation and at the turbulent region y^+ of the first grid point is less than 0.2. During the sensitivity analysis we find that at lower angles of attack, the aerodynamic coefficients have modest variations with respect to the change of the computational grid. At higher angles of attack, when the separation point moves toward the leading edge and the transition abruptly occurs within a short distance, the grid distribution exhibits a significant impact on the computed solution. Grid sensitivity analysis at α=4^o is shown in Table 3. The lift coefficient, except for case 1, which has a grid size of 220×136, varies less than 2%. The drag coefficient shows convergence with grid refinement. The friction drag coefficient is around 0.011 for all the cases. Both the separation position and transition position show convergence pattern too. The same conclusion is also drawn for sensitivity analysis at higher angles of attack. Based on these we surmise that the grid of 220×190 is sufficient. Therefore, we use this grid for all computations reported below.

Effect of Angle of Attack

The lift and drag coefficients at different angles of attack are plotted in Figure 3. Our computed results have a good agreement with the experimental ones at lower angles of attack. Both our simulation and the measurement by Ol et al. [41] predict that the maximum lift coefficient happens at 11^o. Close to stall, our simulations over-predict the lift coefficients. We speculate that at lower angles of attack, when the boundary layer remains thin, the requirements to using e^N are met and the simulation accurately models the physics, while at higher angles of attack, these requirements are no longer met. In general, the numerical results have a good agreement with experimental measurements by Ol et al. [41] and by Selig et al.[34].

At zero angle of attack, laminar separation occurs on the upper surface at about 77% chord position. Because the adverse pressure gradient is modest, the separated flow is able to reattach to the surface at 93% chord position and forms a thin laminar separation bubble (less than 1% of chord length). However, the flow remains laminar in the entire domain. As the angle of attack increases, as illustrated in Figure 4 the adverse pressure gradient downstream of the point of suction peak becomes stronger and the separation point moves toward the leading edge. The stronger pressure gradient amplifies the disturbance in the separation zone and prompts transition. As the turbulence develops, the increased entrainment causes reattachment.[60] At angle of attack of two degree, the separation position is at around 37% chord position and transition occurs at 75% of chord position. A long laminar separation bubble forms. The plateau of the pressure distribution shown in

Figure 4(a) is characteristic of laminar separation bubble. It is also noticed from Figure 4(b) that the bubble length decreases with the increase of angle of attack.

Table 3. Grid Sensitivity Analysis for $\alpha=4^o$ and N=8

Case	Grid Size	C_L	C_D	C_{Df}	Separation position x_s/c	Transition position x_T/c
1	220×136	0.55	0.024	0.010	0.20	0.47
2	330×136	0.62	0.024	0.010	0.20	0.47
3	640×136	0.61	0.023	0.011	0.21	0.48
4	220×190	0.60	0.023	0.011	0.21	0.51
5	330×190	0.61	0.023	0.011	0.21	0.48
6	640×190	0.61	0.024	0.011	0.21	0.48

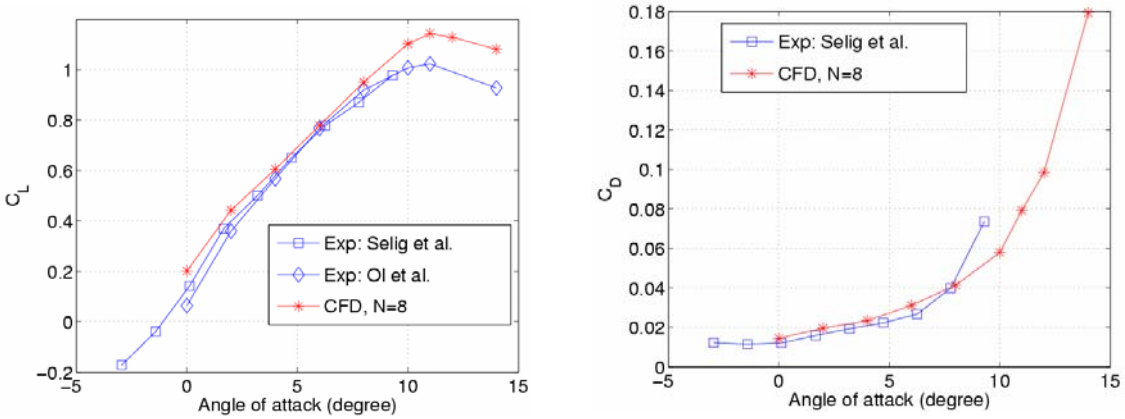

Figure 3. Lift and drag coefficients vs. angle of attack for SD7003 airfoil at Re=6×10^4.

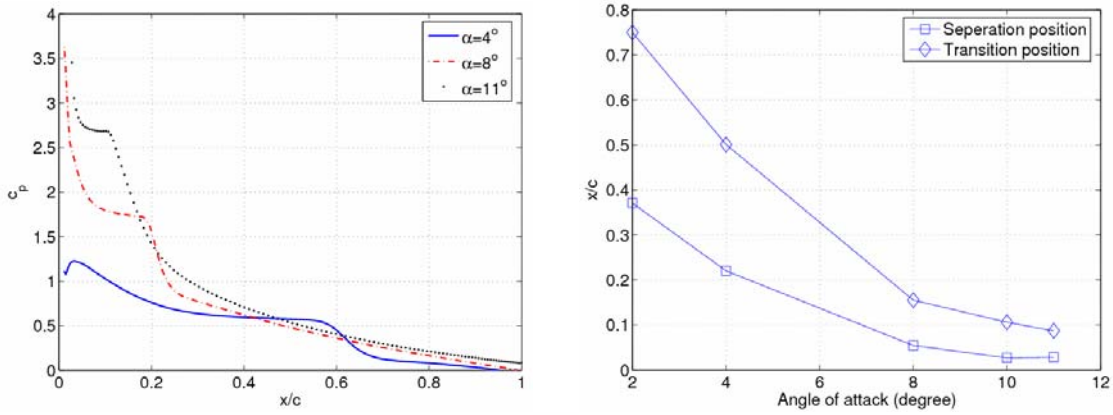

(a) (b)

Figure 4. (a) Pressure coefficients vs. angle of attack; (b) Separation and transition position vs angle of attack for SD7003 airfoil at Re=6×10^4.

The turbulent shear stress, which causes transport of momentum across the boundary layer, is responsible for the closure of the laminar separation bubble. Therefore, it will be helpful and worthwhile to investigate its distribution within the transition region. Radespiel et al. measured the shear stress in the low turbulence wind tunnel (LNB) and the water tunnel (WUB) of the Technical University at Braunschweig.[35] The measurement at $\alpha=4^o$ is performed at LNB. Figure 5 compares the experiment measurement, numerical simulation by Radespiel et al. [35], and our simulation. Radespiel et al. pointed out the due to the low freestream intensity in the experiment, a rather large critical *N*-factor is suitable for the case of $\alpha=4^o$.[35] A critical factor of 10 is adopted in their work and Menter's baseline turbulence model[62] is used. In our simulation, the critical *N*-factor is determined by the correlation previously shown in Eq.(13). Based on the measured turbulence intensity of 0.1%, the critical *N*-factor is set to 8. Our results show that flow experiences transition at 50% of the chord position while the experiment shows transition occurs at 55% of the chord. It should be noted that in the experiment, the transition location is defined as the location where the normalized Reynolds shear stress reaches 0.1% and demonstrates a clearly visible rise. The transition point in our simulation is defined as the point where the most unstable TS wave has amplified over a factor of e^N. If using the normalized shear stress threshold 0.1% as the transition position, the simulated transition point is at 56% of the chord. Overall, as shown in Figure 5, our simulation shows good agreement with the experimental results in terms of transition position, reattachment position, and vortex core position. However, our simulations have noticeably lower shear stress magnitude than the experiment. In all the computations reported here, we have simply followed Eq. (13) to define the transition point, while Radespiel et al.[35] have adjusted the values, making it difficult to predict the aerodynamic performance without experimental validation.

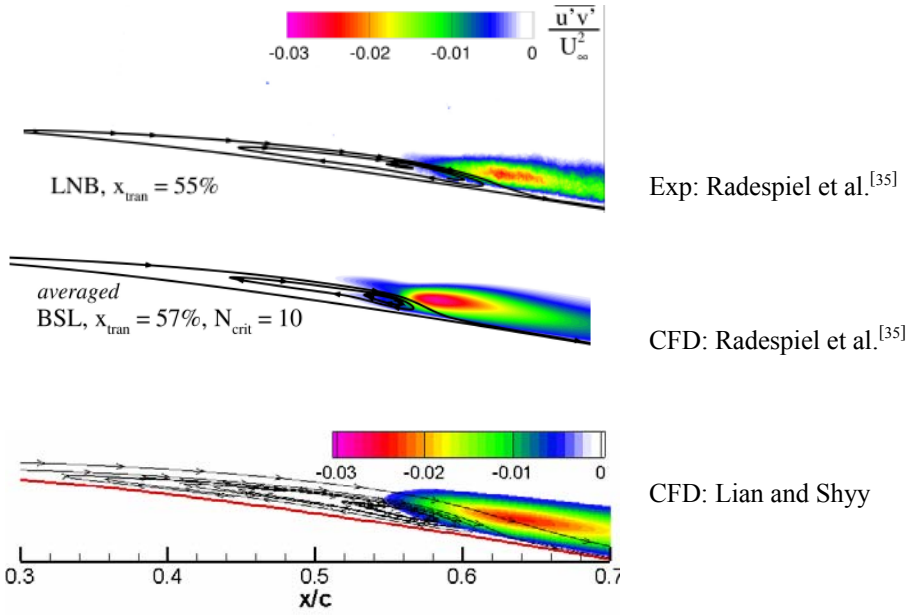

Figure 5.Streamlines and turbulent shear stress for $\alpha=4^o$. From top to bottom: top-Experimental measurement by Radespiel et al.[35]; middle-Numerical simulation by Radespiel et al.[35] with N=10 (plot included with permission from the authors); bottom-present numerical simulation with N=8, which is consistent with the model proposed by Mack.[48]

As the angle of attack increases, both the separation and transition positions move upstream, and the bubble size decreases. At $\alpha=8^o$ the flow separates at 5% of the chord and go though transition at 16%, which is close to the experiment measurement of 14%. The bubble covers approximately 10% of the airfoil chord and it falls into the short bubble category. The computational and experimental results for the $\alpha=8^o$ are shown in Figure 6. The agreement with the experiment one is relatively good. Again, the critical *N*-factor is based on Eq. (13). With critical factor of 8 and Menter's baseline turbulence model,[62] Radespiel et al. predicted that transition took place at 16.5% of chord. The airfoil is close to stall at $\alpha=11^o$, making the case challenging for both experiment and simulation. The separated flow requires a greater pressure recovery in the laminar bubble for reattachment. Otherwise, the bubble becomes long, causing sudden deterioration in airfoil performance. Our simulation predicts flow separates at 5% of the chord, and the separated flow quickly reattaches after it experiences transition at 8.5% chord position, which is close to the measurement of 8.3%. This quick reattachment generally represents the transition-forcing mechanism.[60] Comparison shows that the computed Reynolds shear stress matches the experiment measurement well (Figure 7). With two-layer turbulence model of Menter[62] and a critical factor of 7, Radespiel et al. predicted that transition happened at 8.1% of the chord. [35]

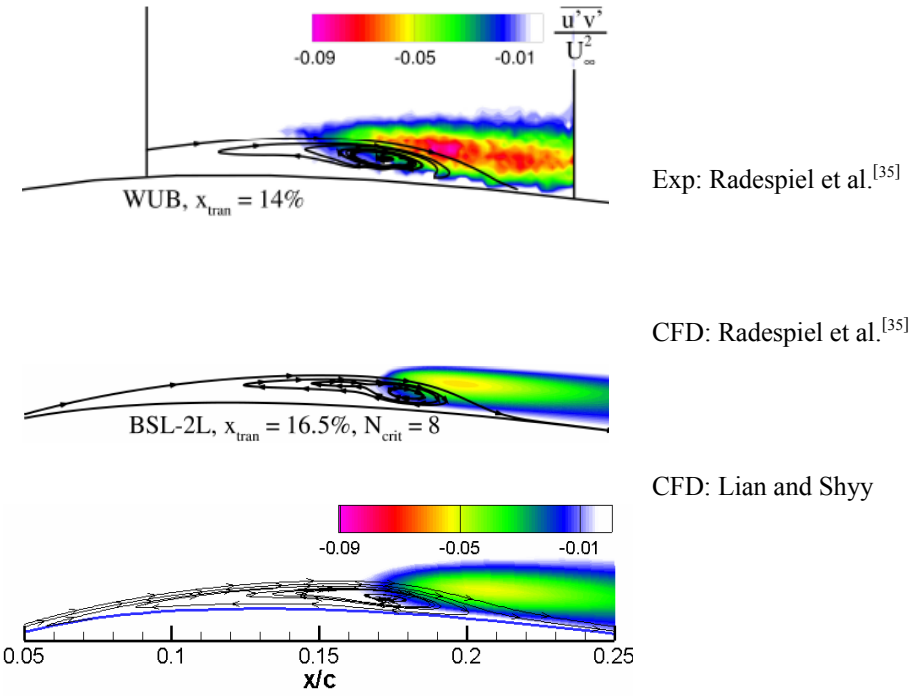

Exp: Radespiel et al.[35]

CFD: Radespiel et al.[35]

CFD: Lian and Shyy

Figure 6.Streamlines and turbulent shear stress for $\alpha=8^o$. From top to bottom: top-Experimental measurement by Radespiel et al.[35]; middle-Numerical simulation by Radespiel et al.[35] with N=8 (plot included with permission from the authors); bottom-present numerical simulation with N=8, which is consistent with the model proposed by Mack.[48]

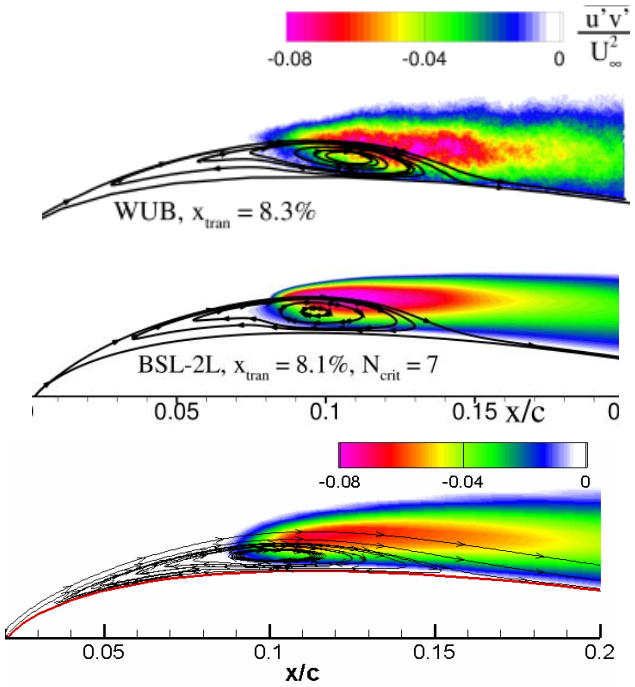

Exp: Radespiel et al.[35]

CFD: Radespiel et al.[35]

CFD: Lian and Shyy

Figure 7.Streamlines and turbulent shear stress for α=11°. From top to bottom: top-Experimental measurement by Radespiel et al.[35]; middle-Numerical simulation by Radespiel et al.[35] with N=7 (plot included with permission from the authors); bottom-present numerical simulation with N=8, which is consistent with the model proposed by Mack.[48]

Effect of freestream turbulence intensity

When both the angle of attack and chord Reynolds number are fixed, generally speaking, as the freestream turbulence level increases, flow experiences earlier transition. Five turbulence levels are chosen in our test. The critical *N*-factor will be adjusted accordingly based on Eq. (13). The lift and drag coefficients are shown in Figure 8. At α=4°, there is no noticeable difference in the lift and drag coefficients among the five tested turbulence levels. This seemingly contradicts the pressure coefficient plot in Figure 9 because the integrated area between c_p=0 and the pressure coefficient plot of *Ti*=0.85% is smaller than that between c_p=0 and the pressure coefficient plot of *Ti*=0.07%. However, the integrated area is not linearly proportional to the lift because of the airfoil curvatures.

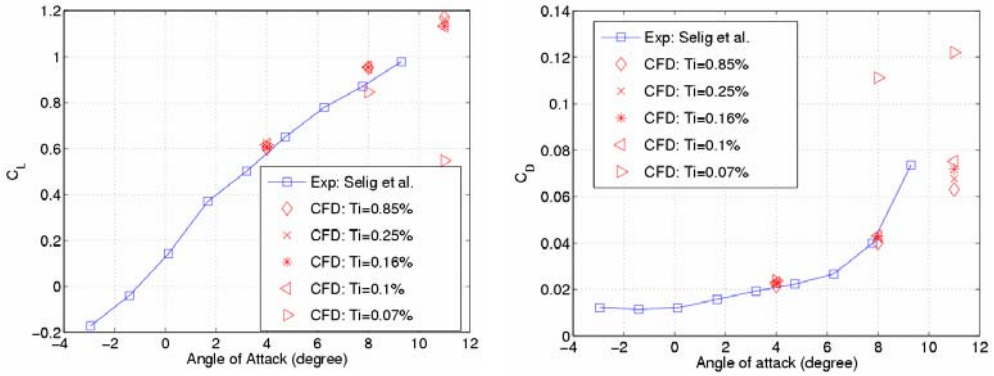

Figure 8. Lift and drag coefficients vs angle of attack at different turbulence levels.

At $\alpha=8^o$, there is a drastic decrease in the lift coefficient and increase in the drag coefficient when *Ti* decreases to 0.07%. Analyzing the flow structure shows that at such a low turbulence level, the flow fails to reattach after the initial separation. This burst separation bubble causes the lift coefficient to drop by 10% and the drag coefficient to increases by more than 150%. Similar conclusion is also made for the case of $\alpha=11^o$.

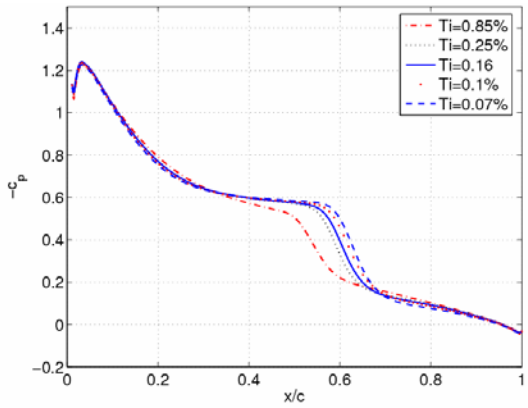

Figure 9. Pressure coefficient on the suction surface at $\alpha=4^o$ at different turbulence levels.

In general with the increase of the freestream turbulence level the LSB becomes thinner and shorter. This is clearly shown in Figure 10. From the same figure we can also see that the shear stress decreases with the turbulence level.

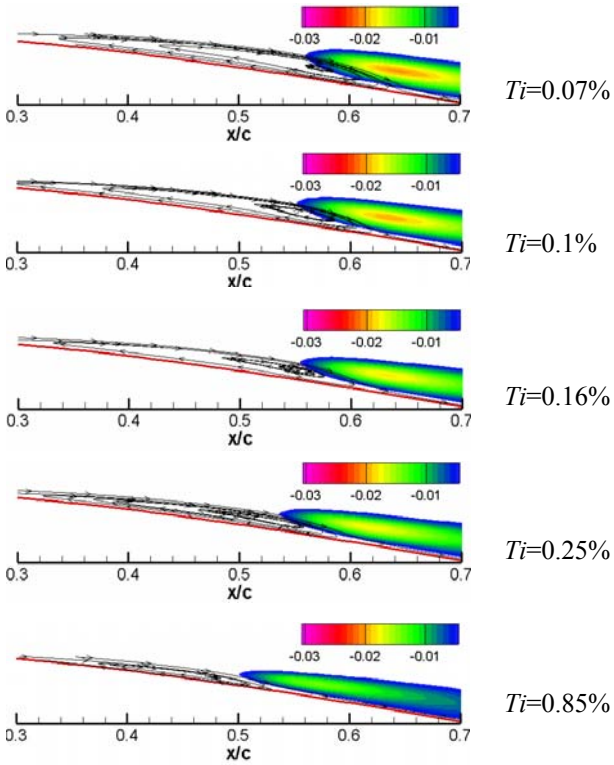

Figure 10. Streamlines and normalized shear stress contours at $\alpha=4^o$ for different turbulence levels.

Because of the viscous effect, the boundary layer and the LSB change the effective shape of the airfoil, which can be approximated by superimposing the viscous displacement thickness on the airfoil. As shown in Figure 11, the flow "feels" a thicker airfoil. The flow with higher turbulence level feels a relatively thinner airfoil than the flow with lower turbulence level.

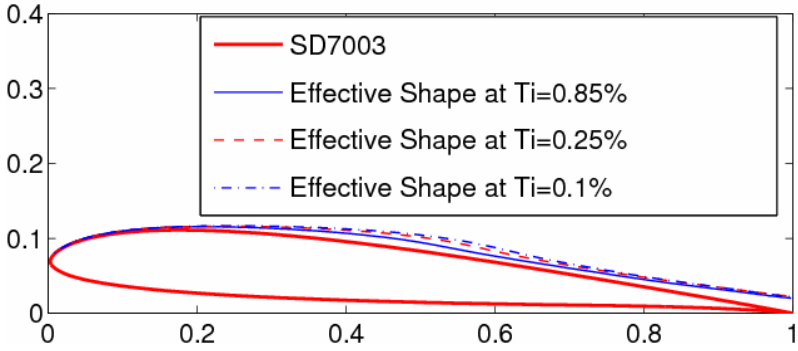

Figure 11. Effective airfoil shape at different turbulence levels.

In their experimental work with a NACA 66_3-018 airfoil, O'Meara and Mueller reported that higher turbulence intensity led to shorter and thinner separation bubble and a higher suction peak.[63] In their study the bubble length is around 7% of chord. For the long bubble reported here, we observe that as the turbulence intensity increase, the bubble decreases in length and thickness. However, we do not find the clear evidence that it can increase the suction peak (Figure 9).

Effect of Reynolds number

For low Reynolds number airfoil, the chord Reynolds number plays a predominated role in the overall performance. As the Reynolds number of the airfoil increases, the Reynolds number based on the momentum thickness increases accordingly. Between the separation position and the transition position, as shown in Figure 12(a), both the shape factor H and the Reynolds number based on the momentum thickness increase with the Reynolds number. Based on Eq. (9) we conclude that the growth rate of the amplification factor before separation increases with the Reynolds number, contributing to earlier transition at higher Reynolds number. Meanwhile, the viscosity changes the effective shape of the airfoil, which is the superimposition of the airfoil and the boundary-layer displacement. Among the studied four cases, as shown in Figure 12(b) the effective airfoil at $Re=4\times10^4$ has the largest camber. This partially explains why the largest lift coefficient is obtained at $Re=4\times10^4$ (Figure 12(c)). The camber decreases significantly when the Reynolds number increases from 4×10^4 to 6×10^4 but does not show considerable change when the Reynolds number increases further. Therefore, we do not observe distinct increase in the lift coefficient even though the LSB length is shorter at higher Reynolds number. We can conclude from Figure 12(d) that the enhancement of lift-to-drag ratio is mainly due to the reduction of friction drag at high Reynolds number. The form drag due to the pressure does not vary as much as the friction drag as the Reynolds number increases. In the application of MAVs, the enhanced lift-to-drag ratio will favor the power efficiency,[8] which is a function of lift-to-drag ratio and increase with the ratio.

Carmichael pointed out that roughly the distance from separation to reattachment can be expressed as a Reynolds number based on the bubble length of about 50,000.[61] A critical Reynolds number of 70,000 is generally accepted based on observation.[60] The evidences collected so far suggest that the transition, separation, and reattachment characteristics are highly dependent on the geometry and angles of attack.

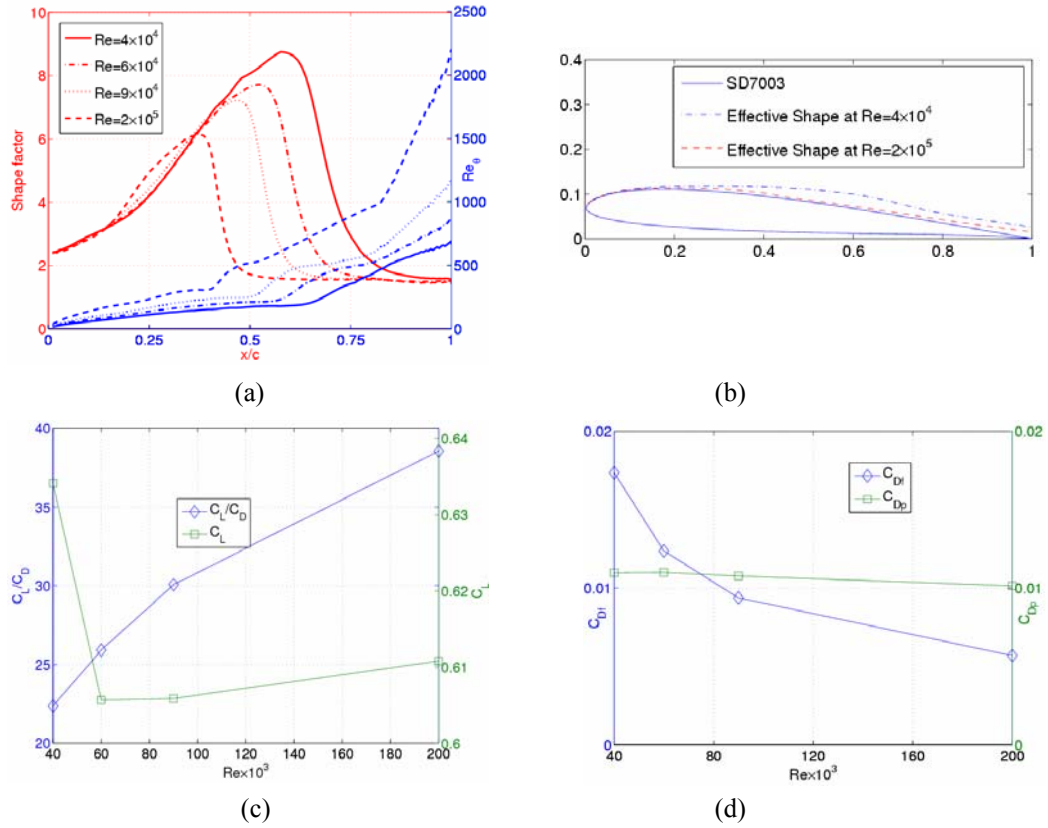

Figure 12. Reynolds number effect on the LSB profile and aerodynamic performance α=4°: (a) Shape factor and momentum thickness based Reynolds number; (b) Effective airfoil shape; (c) lift-to-drag ratio; (d) drag coefficient.

Effect of Gust

The real operating condition for MAVs is quite different from the ideally quite wind/water tunnel setup. In real flight MAVs may have to operate in gusty environment. The effect of unsteady flow on transition was studied by Obremski and Fejer.[64] They experimented with a flat-plate airflow whose freestream velocity varies sinusoidally with a mean:

$$U = U_0(1 + N_A \sin \omega t), \tag{19}$$

where N_A is the amplitude ratio and ω is the frequency. They found experimentally that the transition Reynolds number is affected by the freestream oscillation when the so called "non-steady Reynolds number", $\mathrm{Re}_{ns} = N_A U_0^2 / \omega\nu$, is above a critical point of about 26,000. Below the critical value of the Re_{ns}, the unsteady freestream exhibits little impact on the transition Reynolds number. Obremski and Morkovin[65] observed that in both high and low Re_{ns} ranges, the initial turbulent bursts were preceded in space and time by a disturbance wave packet. By applying a quasi-steady stability model, they concluded that in the high Re_{ns} range the wave packet amplified rapidly and burst into turbulence, whereas in the low range the wave packet burst into turbulence at much higher Reynolds number. Guided by their study, we investigate the influence of freestream oscillations on the transition for separated flows. First, we set N_A=0.33 and ω=0.3, resulting in a Strouhal number of 0.0318 and non-steady Reynolds number of 99,000. The frequency ω is kept well below the range of expected unstable TS wave frequency around 10 Hz. For an airfoil of 15 cm and flies in the air

with speed of 8.3 m/s, if we choose the Strouhal number of 0.0318, the corresponding gust frequency is around 1.75 Hz.

Figure 13 shows the lift coefficient and lift-to-drag ratio during one selected cycle. Clearly, under gust situation, the aerodynamic parameters display the hysteresis. For example, when flow accelerates from $Re=6\times10^4$ to $Re=8\times10^4$, the lift coefficient does not immediately reach its corresponding steady state value. Instead, the steady state value is reached in the decelerating stage. Compared with steady incoming flow, the gust leads to a higher lift coefficient at the low velocity end and lower lift coefficient at high velocity end. The lift-to-drag ratio variation during one cycle is substantial. For example, at the Reynolds number of 6×10^4, the lift-to-drag ratio with a steady state freestream is around 26; for gust flow, the instantaneous lift-to-drag ratio reduces to 20 when the flow accelerates, but elevates to 38 when the flow decelerates.

Along with the variations in lift and drag, the transition position is also affected by the gust. As shown in Figure 14, the transition position moves toward the leading edge when the flow is accelerating and moves toward the trailing edge when flow is decelerating. During the accelerating stage, the instantaneous Reynolds number is increasing. As the Reynolds number increases, flow experiences early transition. In our simulation, we link the transition point to the computational grid point and we do not differentiate any position in between, which makes the plot in Figure 14 discontinuous. And a refined grid will help smooth out the discontinuity.

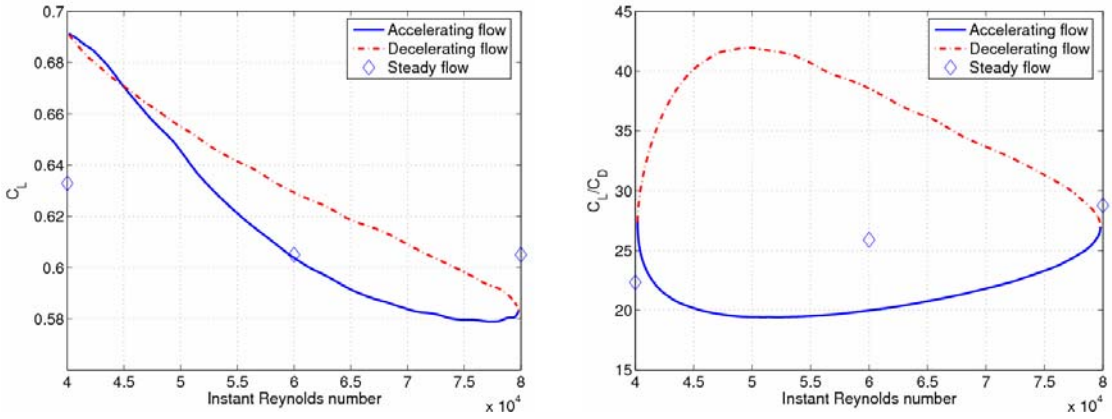

Figure 13. Aerodynamic coefficient in gusty environment during one cycle for Re_{ns}=99,000, showing hyterisis phenomenon. Left: Lift coefficient; Right: Lift-to-drag ratio.

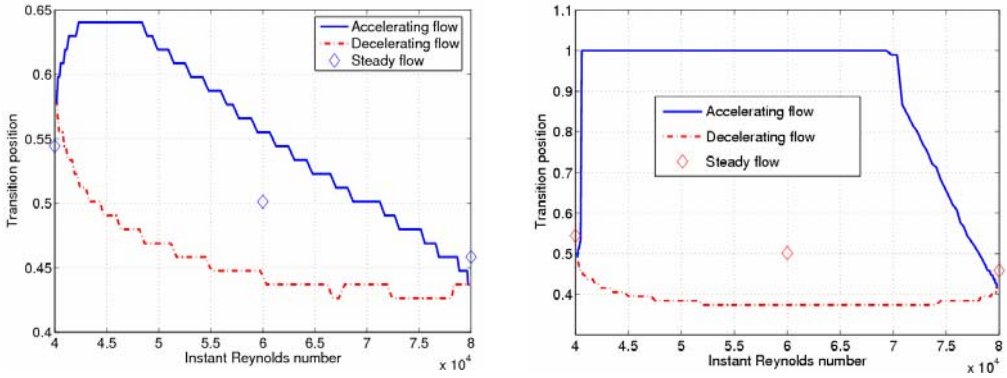

Figure 14. Transition position during one cycle. Left: Re_{ns}=99,000; Right: Re_{ns}=19,800.

We also perform test with a higher frequency of ω=1.5, five times higher than the previous case, resulting in a non-steady Reynolds number of 19,800, which is lower than the critical value. Our numerical result shows that the transition position varies with the instant Reynolds number (Figure 14). This seemingly contradicts the observation of Obremski and Morkovin.[65] However, it should be noted that Obremski and Morkovin draw the conclusion based on experiment over a flat plate at high Reynolds number (10^6), in which flow is the Blasius flow and experiences natural transition. In our test, the separated flow amplifies the unstable TS wave in such a great rate that it results in faster transition to turbulence, typical of the bypass transition scenario.

Comparison of the transition position at the two different non-steady Reynolds numbers reveals that flow experiences transition for the whole oscillation cycle at higher non-steady Reynolds number, while at the lower value the flow becomes laminar at the early accelerating state and remains such until the instant Reynolds number reaches around 7×10^4. We surmise during the decelerating stage, the transition position moves toward the trailing edge due to the lowered Reynolds number. At higher non-steady Reynolds number, i.e., lower frequency, the deceleration has less impact on the transition and the LSB can sustain itself; at lower non-steady Reynolds number, i.e., higher frequency, the deceleration has more impact on the transition and the LSB can not adjust itself with the high rate change to maintain the closed bubble and LSB bursts. A closed LSB forms only when the Reynolds number reaches 7×10^4. To better appreciate this phenomenon, we plot the phase and shape factor during one cycle in Figure 15.

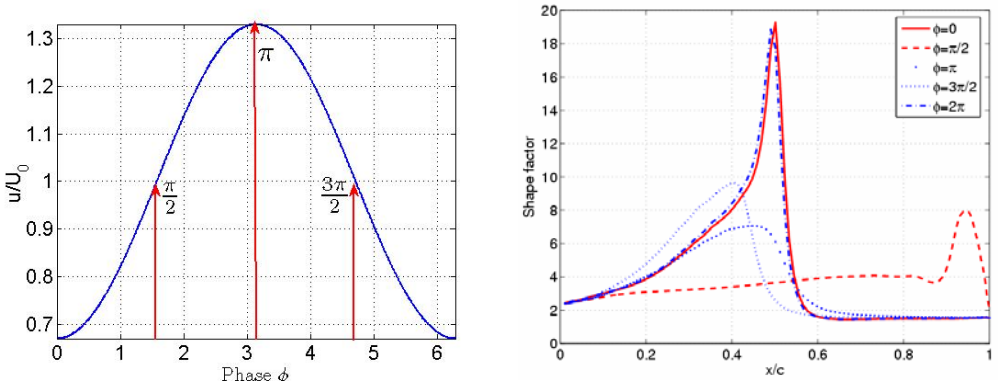

Figure 15. Phase and shape factor during one cycle Re_{ns}=19,800. Left: Phase; Right: Shape factor.

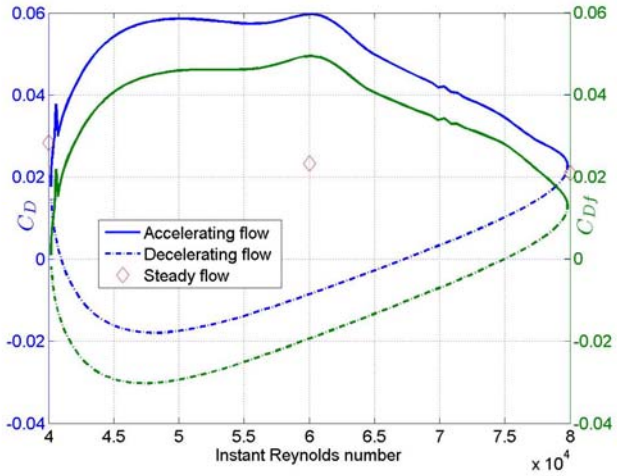

Figure 16. Drag coefficient in gusty environment during one cycle for Re_{ns}=19,800.

Another interesting observation at Re_{ns}=19,800 is the drag coefficient shown in Figure 16. During the decelerating stage the gusty flow produces thrust. Analysis shows that the thrust is due to the friction force. This phenomenon is similar to that observed in the plunging airfoil which can produce thrust at certain combination of frequency and amplitude.[4]

Flexible Wing Simulation

The upper surface of the airfoil is covered with the membrane, which extends from 33% to 52% of the chord (Figure 17). No pretension is applied to the membrane. The membrane has a uniform thickness of 0.2mm with a density of 1200kg/m^3. The two parameters governing the membrane property, as shown in Eq. (16), take the values of c_1=5.0×10^5 pa and c_2=0.785c_1. We simulate the fluid and structure interaction by integrating the fluid and structural solvers previously discussed. Each solver functions independently with its own computational grid and time step, the coupling is accomplished by exchanging information through an interface. As already mentioned, the refernce scales of our computations are based on the freestream velocity, U_0, of 0.3 m/s, and an airfoil chord length of 20 cm. With these parameters, the time step for the CFD solver here is set to 2×10^{-3} second and the time step of the structural solver is 1×10^{-5} second. The structural solver is very fast and the majority CPU time is for the CFD solver. The use of iteration between the CFD solver and structural solver during each time step allows for synchronization of the fluid and structure coupling. By doing this the errors introduced by a lagged fluid/structure coupling approach are regulated.

The test is performed at α=4^o and Re=6×10^4. It is observed that when flow passes the flexible surface, the surface experiences self-excited oscillation and the airfoil displays varied shape over time (Figure 17). Analysis shows that the transverse velocity magnitude can reach as much as 10% of the freestream speed. During the vibration, energy is transferred from the wall to the flow and the separated flow is energized. Compared with corresponding rigid airfoil simulation, the surface vibration causes both the separation and transition positions to exhibit a standard variation of six percent of the chord. Recall our preceding discussion on the impacts of turbulence intensity and Reynolds number, the change of transition position will change the overall aerodynamic performance. Figure 18 shows the time history of the lift coefficient. Even though the time-averaged lift coefficient (0.60) is equal to the lift coefficient of the corresponding rigid wing, the lift coefficient displays a time-dependent variation with maximum magnitude as much as 10% of its mean. The drag coefficient shows similar pattern but the time-averaged value closely matches the rigid wing. These observations are consistent with our previous efforts in 3-D MAV wing simulations, without transitional flow models.[11] Furthermore, the experimental evidence also supports that until the stall condition is reached, the membrane and rigid wings exhibit comparable aerodynamic performance. The flexible wing, on the other hand, can delay the stall margin substantially.[10] Using discrete Fourier transformation analysis we find there is a dominated vibration frequency (167 Hz) associated with the membrane wing (Figure 19). In their simulation with laminar flow over a six-inch membrane wing (i.e., the entire wing surface is flexible), Lian and Shyy also observe this self-vibration with a frequency around 120 Hz,[11] which is comparable to the experimental measurement of 140 Hz. Given the airfoil chord (0.2 m) and freestream speed (0.3 m/s), this high vibration frequency is unlikely to affect the vehicle stability. A close investigation of Figure 18 reveals that besides the high frequency behavior there is low a frequency cycle in the lift coefficient history. This cycle, with a frequency of about 14 Hz, seems to be associated with the periodic vortex shedding (Figure 20).

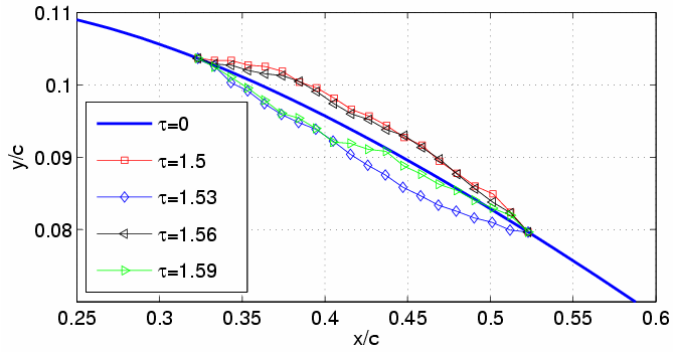

Figure 17. Membrane airfoil shapes at different time instants.

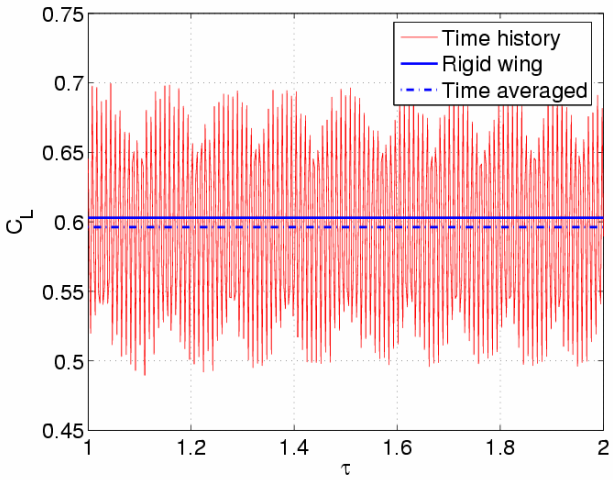

Figure 18. Time history of lift coefficient for membrane wing: showing both a high and low frequency oscillation. τ is the non-dimensionlized time and is equal to tc/U.

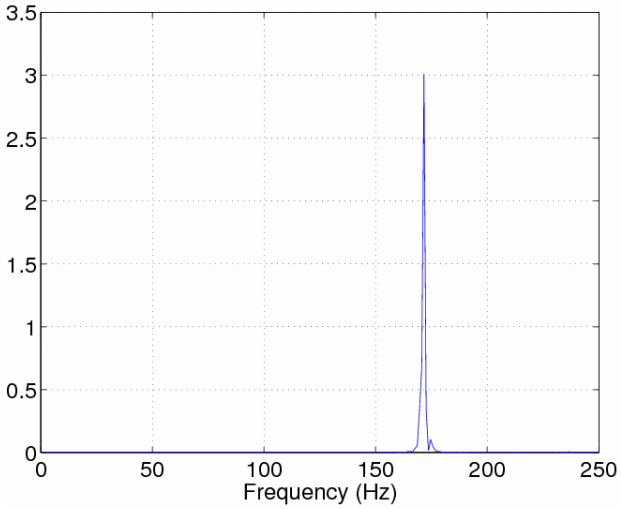

Figure 19. Power spectrum of the Fourier transformation of the lift force.

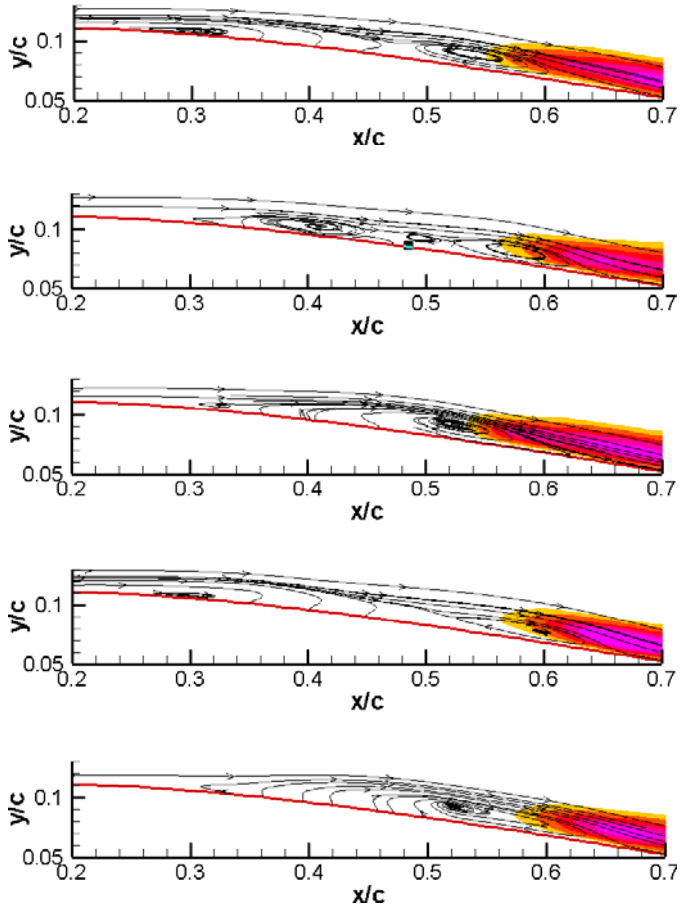

Figure 20. Flow structure over the membrane wing and the associated vortex shedding at $\alpha=4^o$ and Re=60,000. (From top to bottom the time instant τ=1.5, 1.506, 1.512, 1.515, 1.521).

Summary and Conclusion

We coupled a Navier-Stokes equation solver with a transition model and a Reynolds-averaged two-equation closure to study the low Reynolds number flow characterized with laminar separation and transition. The transition model is based on the e^N method, derived from the linear stability analysis and Orr-Sommerfeld equations. An intermittency distribution function suitable for low Reynolds number transitional flow is proposed and tested. With the developed capability we studied the impacts of different factor on transition process and on the airfoil performance. We observed the following:

1) Good agreement between the prediction and experimental measurements regarding the transition location and overall flow structures is observed.

2) As expected, both the separation position and transition position move upstream with increasing angle of attack. The stronger adverse pressure gradient amplifies the unstable TS wave and expedites the transition. Before stall, the laminar separation bubble becomes shorter and thinner with the increase of angle of attack.

3) Increased freestream turbulence intensity prompts the transition, resulting in a shorter and thinner separation bubble. Increased turbulence intensity also leads to higher pressure and velocity peak.

4) Inspecting the flow characteristics between Re = $4x10^4$ and $2x10^5$, one can clearly observe that the actual value of the Reynolds number plays a significant role in the overall airfoil performance. It has similar impacts as the turbulence intensity. For the studied airfoil, though increasing the Reynolds number can shorten the laminar separation bubble, it does not necessarily increase the lift or decrease the drag.

5) The transition position is affected by the gust. When flow accelerates/decelerates, the transition position moves upstream/downstream due to the increasing/decreasing Reynolds number. In the meantime, the lift coefficient demonstrates hysterisis correspond to the acceleration and deceleration process.

6) For a flexible wing, self-excited vibration around 167 Hz is exhibited. During the vibration process, energy is transferred from the flexible surface to the fluid flow, causing the change of flow pattern. Both the separation and transition positions are affected by the vibration. However, at $\alpha=4^o$, the time-averaged lift and drag coefficients are close to those of the steady state flow around the rigid airfoil. Of course, the frequency of gust, the position of the flexible surface, and the membrane property are critical factors in the transition process. These aspects should be further investigated.

Acknowledgment

The present work has been supported by AFOSR.

References

[1]Grasmeyer, J.M. and Keennon, M.T., "Development of the Black Widow Micro Air Vehicle," AIAA Paper No. 2001-0127, 2001.

[2]Ifju, P. G., Jenkins, A. D., Ettingers, S., Lian, Y., and Shyy, W., "Flexible-Wing-Based Micro Air Vehicles," AIAA Paper 2002-0705.

[3]Jones, K. D., Bradshaw, C. J., Papadopoulos, J., and Platzer, M. F., "Improved Performance and Control of Flapping-Wing Propelled Micro Air Vehicles," AIAA Paper 2004-0399.

[4]Jones, K. D., and Platzer, M. F., "Experimental Investigation of the Aerodynamic Characteristics of Flapping-Wing Micro Air Vehicles," AIAA Paper 2003-0418.

[5]Jones, B. M., "Stalling," *J. R. Aero. Soc.*, Vol. 38, pp. 747-770, 1938

[6]Young, A. D., and Horton, H. P., "Some Results of Investigation of Separation Bubbles," AGARD CP, Vol. 4, pp. 779-811, 1966.

[7]Tani, I., "Low Speed Flows Involving Bubble Separations," *Progress in Aeronautical Science*, Pergamon Press, pp. 70-103, 1964.

[8]Shyy, W., Berg, M., and Ljungqvist D., "Flapping and Flexible Wings for Biological and MicroVehicles," *Prog. Aerospace Science*, 35, pp. 455-506, 1999.

[9]Lian, Y., Shyy, W., Viieru, D., and Zhang, B. N., "Membrane Wing Aerodynamics for Micro Air Vehicles," *Progress in Aerospace Sciences*, Vol. 39, 2003, pp. 425-465.

[10]Waszak, R. M., Jenkins, N. L., and Ifju, P., "Stability and Control Properties of an Aeroelastic Fixed Wing Micro Aerial Vehicle," AIAA Paper 2001-4005, presented at the AIAA Atmospheric Flight Mechanics Conference and Exhibit, Montreal, Canada, Aug. 6-9, 2001.

[11]Lian, Y., and Shyy, W., "Numerical Simulations of Membrane Wing Aerodynamics for Micro Air Vehicle Applications," *Journal of Aircraft*, Vol. 42, No. 4, 2005, pp. 865-873.

[12]Smith, A. M. O., and Gamberoni, N., "Transition, Pressure gradient, and Stability Theory," Douglas Aircraft Report ES-26388, 1956.

[13]Van Ingen, J. L., "A Suggested Semi-Empirical Method for the Calculation of the Boundary Layer Transition Region," Inst. of Tech., Dept. of Aeronautics and Engrg., Report VTH-74, Delft, Holland, 1956.

[14]Roberts, W. B., "Calculation of Laminar Separation Bubbles and Their Effect on Airfoil Performance," *AIAA Journal*, Vol. 18, No. 1, pp. 25-31, 1980.

[15]Davis, R. L., Carter, J. E., and Reshotko, E., "Analysis of Transitional Separation Bubbles on Infinite Swept Wings," *AIAA Journal*, Vol. 25. No. 3, pp. 421-428, 1987.

[16]Volino, R. J., and Bohl, D. G., "Separated Flow Transition Mechanism and Prediction with High and Low Freestream Turbulence under Low Pressure Turbine Conditions," ASME paper No. GT2004-53360, 2004.

[17]Mayle, R. E., "The Role of Laminar-Turbulent Transition in Gas Turbine Engine," *Journal of Turbomachinery*, Vol. 113, pp. 509-537, 1991.

[18]Praisner, T. J., and Clark, J. P., "Predicting Transition in Turbomachinery, Part I-A Review and New Model Development," ASME Paper No. GT2004-54108, 2004.

[19]Roberts, S. K., and Yaras, M. I., "Effects of Surface Roughness Geometry on Separation Bubble Transition," ASME Paper No. GT2005-68664, 2005.

[20]Wazzan, A. R., Gazley, C., Jr., and Smith, A. M. O., "Tollmien-Schlichting Waves and Transition," *Prog. Aerosp. Sci.*, Vol. 18, No. 2, pp. 351-392, 1979.

[21]He, X., Senocak, I., Shyy, W., Gangadharan, S. N., and Thakur, S., "Evaluation of Laminar-turbulent Transition and Equilibrium Near Wall Turbulence Models," *Numerical Heat Transfer, Part A*, Vol. 37, pp. 101-112, 2000.

[22]Cebeci, T., "Essential Ingredients of a Method for Low Reynolds-Number Airfoils," *AIAA Journal*, Vol. 27, No. 12, pp. 1680-1688, 1988.

[23]Drela, M., and Giles, M. B., "Viscous-Inviscid Analysis of Transonic and Low Reynolds Number Airfoils," *AIAA Journal*, Vol. 23, No. 10, pp. 1347-1355, 1987.

[24]Holloway, D. S., Walters, D. K., and Leylek, J. H., "Prediction of Unsteady, Separated Boundary Layer over a Blunt Body for Laminar, Turbulent, and Transitional Flow," *International Journal for Numerical Methods in Fluids*, Vol. 45, pp. 1291-1315, 2004.

[25]Dick, E., and Steelant, J., "Coupled Solution of the Steady Compressible Navier-Stokes equations and the k-ε turbulence equations with a multigrid method," *Appl. Numer. Math*, Vol. 23, pp. 49-61, 1997.

[26]Edwards, J. R., Roy, C. J., Blottner, F. G., and Hassan, H. A., "Development of a One-Equation Transition/Turbulence Model," *AIAA Journal*, Vol. 39, No. 9, pp. 1691-1698, 2001.

[27]Warren, E. S., and Hassan, H. A., "Transition Closure Model for Predicting Transition Onset," *Journal of Aircraft*, Vol. 35, No. 5, pp. 769-775, 1998.

[28]Spalart, P. R., and Allmaras, S. R., "A One-Equation Turbulence Model for Aerodynamic Flow," *La Recherche Aerospatiale*, Vol. 1, pp. 5-21, 1994.

[29]Wilcox, D. C., "Simulation of Transition with a Two-Equation Turbulence Model," *AIAA J.*, Vol. 32, No. 2, pp. 247-255, 1994.

[30]Steelant, J., and Dick, E., "Modeling of Bypass Transition with Conditioned Navier-Stokes Equations Coupled to an Intermittency Transport Equation," *Int. J. Numer. Mech. Fluids*, Vol. 23, pp. 193-220, 1996.

[31]Suen, Y. B., and Huang, P. G., "Modeling of Flow Transition Using an Intermittency Transport Equation," *Journal of Fluid Engineering*, Vol. 122, pp. 273-284, 2000.

[32]Suen, Y. B., Xiong, G., and Huang, P. G., "Predictions of Transitional Flows in Low-Pressure Turbines Using Intermittency Transport Equation," *AIAA Journal*, Vol. 40, No. 2, pp. 254-266, 2002.

[33]Zheng, X., Liu, C., Liu, F., and Yang, C., Turbulence Transition Simulation Using The K-w Model, *Int. J. Numer. Mech. Engng.*, Vol. 42, pp. 907-926, 1998.

[34]Selig, M. S., Guglielmo, J. J., Broeren, A. P., and Giguere, P., *Summary of Low-Speed Airfoil Data*-Vol. 1, Soartech Publication, 1995.

[35]Radespiel, R., Graage, K., and Brodersen, O., "Transition Predictions Using Reynolds-Averaged Navier-Stokes and Linear Stability Analysis Methods," AIAA Paper 91-1641, June 1991.

[36]Stock, H. W., and Haase, W., "A Feasibility Study of e^N Transition Prediction in Navier-Stokes Methods for Airfoils," *AIAA Journal*, Vol. 37, No. 10, pp. 1187-1196, 1999.

[37]Yuan, W., Khalid, M., Windte, J., Scholz, U., and Radespiel, R., "An Investigation of Low-Reynolds-Number Flows Past Airfoils," AIAA Paper 2005-4607, 23rd AIAA Applied Aerodynamics Conference, Toronto, June 6-9, 2005.

[38]Arnal, D., Casalis, G., and Juillen, J. C., "A Survey of the Transition Prediction Methods: from Analytical Criteria to PSE and DNS," in M. Hallback (ed.) *Turbulence and Transition Modeling*, Lecture Notes from the ERCOFTAC/IUTAM Summer School held in Stockholm, June 12-20, 1995, Kluwer Academic Publishers, Dordrecht, pp. 3-14, 1996.

[39]Strelets, M., "Detached Eddy Simulation of Massively Separated Flows," AIAA Paper 2001-0879.

[40]Yang, Z., and Voke, P., "Large Eddy Simulation of Boundary-Layer Separation and Transition at a Change of Surface Curvature," *J. Fluid Mech.* Vol. 439, pp. 305-333, 2001.

[41]Ol, M., McAuliffe, B. R., Hanff, E. S., Scholz, U., and Kaehler, C., "Comparison of Laminar Separation Bubble Measurements on a Low Reynolds Number Airfoil in Three Facilities," AIAA Paper 2005-5149, 23rd AIAA Applied Aerodynamics Conference, Toronto, June 6-9, 2005.

[42]Hanff, E. S., "PIV Application in Advanced Low Reynolds Number Facility," *IEEE Aerospace and Electronic Systems*, Vol. 40, pp. 310-319, 2004.

[43]Nerger, D., Kähler, C. J., and Radespiel, R., "Zeitaufgelöste PIV-Messungen an einem schwingenden SD7003-Profil bei Re=60000", *Lasermethoden in der Strömungsmesstechnik*, 11. GALA Fachtagung, 9.-11. September, Braunschweig, 2003.

[44]Patankar, S. V., and Spalding, D. B., "A Calculation Procedure for Heat, Mass and Momentum Transfer in Three-dimensional Parabolic Flows," *Int. J. Heat Mass Transfer*, Vol. 15, pp. 1787-1806, 1972.

[45]Shyy, W., *Computational Modeling for Fluid Flow and Interfacial Transport*, Elsevier, Amsterdam, The Netherlands, (1994, revised printing 1997) xviii+504 pages.

[46]Wilcox, D., *Turbulence Modeling for CFD* (Second Edition), DCW Industries, Inc, La Canada, California, 2000.

[47]Gleyzes, C., Cousteix, Jr. and Bonnet, J. L., "Theoretical and Experimental Study of Low Reynolds Number Transitional Separation Bubbles," Presented at the Conference on Low Reynolds Number Airfoil Aerodynamics, University of Notre Dame, Notre Dame, IN, 1985.

[48]Mack, L. M., "Transition Prediction and Linear Stability Theory," pp. 1-1-1-22 of AGARD, 1977.

[49]van Ingen, J. L., "Some Introductory Remarks on Transition Prediction Methods Based on Linear Stability Theory," In: *Proceedings of the colloquium Transitional Boundary Layers in Aeronautics* (edited by Henkes, R.R.W.M., and van Ingen, J. L.), North-Holland, New York, pp. 209-224, 1996.

[50]Dhawan, S., and Narasimha, R., "Some Properties of Boundary Layer During the Transition from Laminar to Turbulent Flow Motion," *Journal of Fluid Mechanics*, Vol. 3, pp. 418-436, 1958.

[51]Cebeci, T., "Essential Ingredients of a Method for Low Reynolds-Number Airfoils," *AIAA Journal,* Vol. 27, No. 12, pp. 1680-1688, 1988.

[52]Chen, K. K., and Thyson, N. A., "Extension of Emmons' Spot Theory to Flows on Blunt Bodies," *AIAA Journal*, Vol. 9, pp. 821-825, 1971.

[53]Lian, Y., Shyy, W., Ifju, P., and Verron, E., "A Membrane Wing Model for Micro Air Vehicles," *AIAA Journal*, Vol. 41, 2003, pp. 2492-2494, also AIAA Paper 2002-2972.

[54]Green, A. E., Adkins, J. E., *Large Elastic Deformations*, the Clarendon Press, Oxford, 1960.

[55]Mooney, M., "A Theory of Large Elastic Deformation," *Journal of Applied Physics*, Vol. 11, pp. 582-592.

[56]Bathe, K. J., *Finite Element Procedures*, Prentice Hall, Englewood, New Jersey, 1996.

[57]Lian, Y., Steen, J., Trygg-Wilander, M., and Shyy, W., "Low Reynolds Number Turbulent Flows around a Dynamically Shaped Airfoil," *Computers and Fluids*, Vol. 32, 2003, pp. 287-303. Also AIAA Paper 2001-2723.

[58]Visbal, M. R., and Gaitonde, D. V., "On the Use of Higher-Order Finite-Difference Schemes on Curvilinear and Deforming Meshes," *Journal of Computational Physics*, Vol. 181, pp. 155-185, 2002.

[59]Thomas, P. D., and Lombard, C. K., "Geometric Conservation Law and its Application to Flow Computations on Moving Grids," *AIAA Journal*, Vol. 17, No. 10, pp. 1030-1037, 1979.

[60]Lissaman, P. B. S., "Low Reynolds-Number Airfoils," *Ann. Rev. Fluid Mech*. Vol. 15, pp. 223-239, 1983.

[61]Carmichael, B. H., "Low Reynolds Number Airfoil Survey," Vol. 1. NASA CR 165803, 1981.

[62]Menter, F. R., "Two-equation Eddy-viscosity Transport Turbulence Model for Engineering Applications," *AIAA Journal,* Vol. 32, No. 8, pp. 1598-1605, 1994.

[63]O'Meara, M. M., and Mueller, T. J., "Laminar Separation Bubble Characteristics on an Airfoil at Low Reynolds Numbers," *AIAA Journal*, Vol. 25, No. 8, pp. 1033-1041, 1987.

[64]Obremski, H. J., and Fejer, A. A., "Transition in Oscillating Boundary Layer Flow," *Journal of Fluid Mechanics*, Vol. 29, pp. 93-111, 1967.

[65]Obremski, H. J., and Morkovin, M. V., "Application of a Quasi-Steady Stability Model to Periodic Boundary Layer Flows," *AIAA Journal*, Vol. 7, No. 7, pp. 1298-1301, 1969.